CrossMark

Flow criticality governs leading-edge-vortex initiation on finite wings in unsteady flow

**Yoshikazu Hirato[1], Minao Shen[1], Ashok Gopalarathnam[1],†
and Jack R. Edwards[1]**

[1]Department of Mechanical and Aerospace Engineering, North Carolina State University,
Raleigh, NC 27695, USA

Leading-edge-vortex (LEV) formation often characterizes the unsteady flows past airfoils and wings. Recent research showed that initiation of LEV formation on airfoils in two-dimensional flow is closely tied to the criticality of the so-called leading-edge suction parameter (LESP). To characterize the LEV initiation on wings in three-dimensional flow, a large set of pitching wings was studied using Reynolds-averaged Navier–Stokes computations (computational fluid dynamics, CFD). The CFD results showed that the pitch angle and spanwise location for LEV initiation varied widely between the different wings. The same cases were also analysed using an unsteady vortex-lattice method (UVLM), which assumes attached flow. Low-order prediction of LEV initiation is assumed to occur at the pitch angle when the UVLM-calculated LESP at any point on the wing span first becomes equal to the pre-determined critical LESP for the airfoil. For all the cases, the predicted pitch angles and spanwise locations for LEV initiation from the low-order method agreed excellently with the corresponding CFD predictions. These observations show that LEV initiation on finite wings is governed by criticality of leading-edge suction, enabling the prediction of LEV initiation on an unsteady finite wing using attached-flow wing theory and the critical LESP values for the airfoil sections.

Key words: swimming/flying, vortex shedding, boundary layer separation

1. Introduction

Vortex shedding from the leading edges of foils, wings and rotor blades have been observed in nature – on swimming and flying animals and seeds (Ellington *et al.* 1996; Taylor, Nudds & Thomas 2003; Muijres *et al.* 2008; Lentink *et al.* 2009; Limacher & Rival 2015; Bottom II *et al.* 2016), and in engineering – on rotorcraft (Carr 1988; Corke & Thomas 2015), wind turbines (Schreck & Robinson 2005), swept and delta wings (Maltby 1968; Hitzel & Schmidt 1984; Gursul, Gordnier & Visbal 2005), micro-air vehicles (Ellington *et al.* 1996; Ellington 1999) and flapping-wing energy-harvesting devices (Young, Lai & Platzer 2014). Many investigations of leading-edge-vortex (LEV) formation and shedding from airfoils in two-dimensional flow have revealed the connection between the onset of separation and/or vortex formation at the leading edge and its dependence on leading-edge radius and Reynolds number (McCullough & Gault 1951; Gault 1957; Ham

† Email address for correspondence: agopalar@ncsu.edu

& Garelick 1968), and unsteady motion kinematics of the airfoil (Visbal & Shang 1989; Ghosh Choudhuri & Knight 1996; Granlund, Ol & Bernal 2013). Several computational and experimental studies have shown the effects of the LEV growth, position and detachment on the forces and moments experienced by the airfoil (Ghosh Choudhuri, Knight & Visbal 1994; Ghosh Choudhuri & Knight 1996; Ol 2009). The restriction to two-dimensional flow in airfoil studies enables the use of low-order discrete-vortex methods for modelling the airfoil LEV formation and its effects (Ansari, Żbikowski & Knowles 2006*b*,*a*; Ramesh *et al.* 2014). In contrast, LEV formation, shedding, growth and their effects on finite wings and blades are considerably more complicated due to the presence of spanwise velocities and pressure gradients, rotational effects, interaction with root and tip-vortex structures and the interplay between vorticity production and spanwise/chordwise advection (Maxworthy 1979; Dickinson & Götz 1993; Maxworthy 2007; Harbig, Sheridan & Thompson 2014; Wojcik & Buchholz 2014; Wong & Rival 2015; Limacher, Morton & Wood 2016). On some geometries, such as the highly swept leading edges of delta wings, vorticity production at the leading edges is balanced by spanwise vorticity transport, leading to body-relative stable or stationary vortex structures, which can be harnessed for lift enhancement at high angles of attack and extra manoeuvrability (Rao & Campbell 1987). The effects of these LEV flows are also amenable to simple and elegant theories such as the Polhamus leading-edge suction analogy (Polhamus 1966, 1971). In other configurations, such as unswept wings, the absence of mechanisms for spanwise transport of shed leading-edge vorticity appears to be the cause for non-uniform shedding and chordwise advection, leading to interesting and important flow structures like the omega-shaped (or horseshoe-shaped) vortical structures that have been observed in experiments and computations (Freymuth 1988; Schreck & Helin 1994; Yilmaz & Rockwell 2012; Visbal, Yilmaz & Rockwell 2013; Gordnier & Demasi 2013). Further complicating the three-dimensional situation are the rotational effects on these phenomena on rotor blades and flapping wings (Lentink *et al.* 2009; Lentink & Dickinson 2009; Venkata & Jones 2013; Limacher *et al.* 2016).

Although LEV formation on finite wings is riddled with complexities, it may be argued that the first step in unravelling the flow physics of finite-wing LEVs is to gain insight into the initiation of LEV formation: for any given wing and motion kinematic, at what time or pitch angle and where along the span does the LEV start forming? The current research was focused on answering this specific question. Building on an earlier work on initiation of LEV formation on rounded leading-edge airfoils (Ramesh *et al.* 2014), and using results from three-dimensional computational fluid dynamics (CFD) computations for a large number of finite wings, it is shown that criticality of leading-edge suction, which governs LEV formation on airfoils, can also be reliably used to predict the initiation of LEV formation on finite wings in low-Mach-number flows.

The remainder of the paper begins with a brief review in § 2 of the recently developed low-order prediction method for unsteady airfoils with LEV shedding (Ramesh *et al.* 2014), as the leading-edge suction parameter (LESP) concept introduced in that work provides the foundation for the current study. Section 3 presents the essential details of the unsteady vortex-lattice method (VLM; the low-order method), the Reynolds-averaged Navier–Stokes (RANS) computational method (the high-order method), the airfoil and finite-wing geometries used in this study and the approach used to determine the initiation of LEV formation. The results of the study in § 4 are followed by conclusions in § 5.

2. Background: prediction of LEV shedding on airfoils

Recent progress by Ramesh *et al.* (2014) in the development of a criterion for LEV initiation on unsteady airfoils has provided the impetus for the current work. In that work,

it was shown that, for unsteady airfoils undergoing high-rate motions, the initiation of LEV formation occurs when the instantaneous value of the LESP reaches a critical value, termed LESP$_{crit}$. The instantaneous LESP, which is a non-dimensional parameter that can be calculated in unsteady thin-airfoil theory, provides a measure of the aerodynamic condition at the leading edge (i.e. flow velocity, suction peak and the adverse pressure gradient). It was shown that, so long as the motions considered do not result in significant trailing-edge reversed flow preceding the LEV formation, LESP$_{crit}$ depends only on airfoil shape and Reynolds number, and is largely independent of motion kinematics. Thus, if LESP$_{crit}$ is determined from two-dimensional experiment or CFD for one high-rate motion, it can be used for low-order prediction of LEV initiation for any other high-rate motion. Using this insight, a low-order prediction method, named the LESP-modulated discrete vortex method, or LDVM, was developed.

This section briefly describes (i) the unsteady thin-airfoil theory that is at the foundation of the LDVM code and (ii) the LESP criterion for initiation of LEV formation on airfoils. The interested reader may refer to Ramesh *et al.* (2014) for further details.

2.1. *Large-angle unsteady thin-airfoil theory*

At the foundation of the LDVM is a large-angle unsteady thin-airfoil theory detailed in Ramesh *et al.* (2013). This theory is based on the time-stepping formulation given by Katz & Plotkin (2001), but eliminates the traditional small-angle assumptions in thin-airfoil theory. At each time step, a discrete vortex is shed from the airfoil trailing edge. The vortex-sheet strength distribution, $\gamma(x)$ or $\gamma(\theta)$, over the airfoil at any given time step is taken to be a Fourier series truncated to N terms

$$\gamma(\theta) = 2U_\infty \left[A_0 \frac{1 + \cos\theta}{\sin\theta} + \sum_{n=1}^{N} A_n \sin(n\theta) \right], \qquad (2.1)$$

where the angular coordinate, θ, relates to the chordwise coordinate, x, as: $x = c(1 - \cos\theta)/2$, with x measured from the leading edge; that is, $0 \leqslant x \leqslant c$ and $0 \leqslant \theta \leqslant \pi$, where c is the chord length of the airfoil, $A_0, A_1, \ldots, A_N$ are the time-dependent Fourier coefficients and U_∞ is the free-stream velocity. The Kutta condition (zero vortex-sheet strength at the trailing edge) is enforced implicitly through the form of the Fourier series. The Fourier coefficients are calculated by enforcing the boundary condition of zero normal flow through the airfoil camberline. Force and moments coefficients are calculated using unsteady Bernoulli's theorem (Ramesh *et al.* 2013).

2.2. *Criticality of LESP and LEV shedding on airfoils*

It has been known for several decades that the onset of separation at the leading edge is governed by criticality of flow parameters at the leading edge. Several researchers (Evans & Mort 1959; Beddoes 1978; Ekaterinaris & Platzer 1998; Jones & Platzer 1998; Morris & Rusak 2013) have correlated leading-edge flow criticality to onset of leading-edge separation and/or static/dynamic stall. The LESP idea of Ramesh *et al.* (2014), inspired in part by these works, was the result of the search for an appropriate parameter that could be determined as a part of an unsteady airfoil theoretical calculation.

The LESP is a measure of the suction at the leading edge, which in turn is caused by the stagnation point moving away from the leading edge when the airfoil is at an angle of attack. Ramesh *et al.* observed that the determining factor for the leading-edge suction for an airfoil is the circulation at the leading edge, $\gamma(0, t)$, which is represented by the

first coefficient $A_0(t)$. The instantaneous LESP at any time instant is therefore taken as the value of $A_0(t)$ at that time as follows:

$$LESP(t) = A_0(t). \tag{2.2}$$

As noted by Katz (1981), airfoils having rounded leading edges can support some suction even when the stagnation point is away from the airfoil leading edge. The amount of suction that can be supported is a characteristic of the airfoil shape and Reynolds number of operation. When these quantities are constant, it was shown in Ramesh *et al.* (2014) that initiation of LEV formation always occurred at the same value of LESP regardless of motion kinematics and history, provided the LEV formation was not preceded by significant trailing-edge separation. This threshold value of LESP, which is a function of the airfoil shape and Reynolds number, is termed the critical LESP, or LESP*crit*. This value of LESP*crit*, for any given airfoil and Reynolds number, can be obtained from CFD or experimental predictions for a single motion (Ramesh *et al.* 2014), and can then be used for any other motion to predict LEV formation. In Ramesh *et al.* (2014), this idea was used not only to predict initiation of LEV formation but also to predict subsequent vortex shedding from the leading edge and termination of LEV shedding. The LDVM code handles these events by using discrete-vortex shedding from the leading edge modulated by the difference between the instantaneous value of the LESP at any given time and the critical value.

The idea of the criticality of LESP is extended in the current work to vortex shedding from finite wings, but the emphasis in this paper is only on the initiation of LEV formation.

3. Methodology

3.1. *Unsteady vortex-lattice method*

The unsteady vortex-lattice method (UVLM) is a low-order method that is frequently used for wing and aircraft aerodynamics and aeroelasticity (Murua, Palacios & Graham 2012). The current formulation largely follows the time-stepping approach presented by Katz & Plotkin (2001). This section provides a only brief overview of the method, focusing mainly on the modifications to the standard UVLM as needed for the current research. For further details, the reader is referred to Katz & Plotkin (2001).

In the UVLM, the wing mean-camber surface is discretized into lattices along the wing span and chord, as shown in figure 1. Vortex rings are distributed along this surface; the strengths of these rings, denoted by Γ, are determined by satisfying the zero-normal-flow boundary conditions at control points located at the centres of the rings. As the wing moves in an unsteady motion, vortex rings are shed along the wake. The strengths of the most-recent shed wake rings are determined by satisfying the Kelvin and unsteady Kutta conditions. Once shed, the strengths of the vortex rings in the wake remain unchanged. Aerodynamic load distributions are calculated using the unsteady Bernoulli equation. In the current research, the standard UVLM (Katz & Plotkin 2001) was modified by adding two capabilities: (i) implementation of wake roll-up and 'separated-tip-flow' models as optional features, and (ii) an additional procedure to calculate the spanwise variation of LESP at every time step. The remainder of this subsection discusses these two modifications.

3.1.1. *Wake roll-up and separated-tip-flow models*

The wake roll-up and tip-flow models were added as two optional features to the standard UVLM formulation to assess the effects of wake and tip flows on the LESP
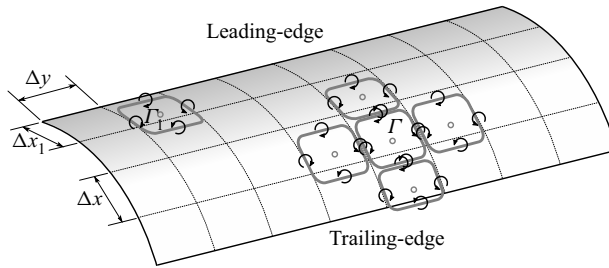
FIGURE 1. Vortex-sheet representation and discretization on a wing mean-camber surface.
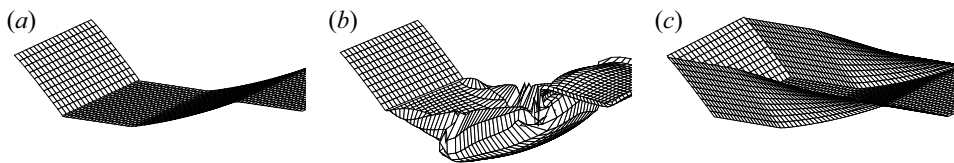

FIGURE 2. Comparison of wake-vortex models in UVLM. (*a*) Attached-tip-flow model (ATFM). (*b*) Attached-tip-flow model with roll up. (*c*) Separated-tip-flow model (STFM).

prediction, especially for low-aspect-ratio (low-AR) wings. Figure 2 compares these models. The standard UVLM implementation with no wake roll up and attached-tip-flow model is shown in figure 2(*a*). With this option, the wake geometry stays unchanged and the vorticity at the wing tips is assumed to be concentrated along the tip edge over the entire tip chord. The option with attached tip flow and wake roll up is illustrated in figure 2(*b*). The procedure for this option is also described in Katz & Plotkin (2001). The wake roll up models a force-free wake in which each wake-vortex element is made to move with the local flow velocity. Although the current implementation of UVLM can handle wake roll up, no significant effect was observed in the loads or the spanwise LESP distributions due to use of the wake roll-up option. For this reason, and because wake roll-up calculations result in a significant increase in computational time, the wake roll-up option was not used in any of the studies in this effort.

The separated-tip-flow option was added to better approximate the behaviour of shed tip vortices on wings. It is known that vorticity shed from a sharp wing tip typically rolls up into a conical vortex structure that flows downstream along the upper surface of the wing tip and merges with the trailing-vortex sheet. An example of such a tip flow is shown later in figure 4. Figure 2(*c*) shows the separated-tip-flow option in the current UVLM code. In this option, vortex rings are released from the tip edges similar to how the wake vortex rings are released from the trailing edge in the standard UVLM. It is clear that, to correctly model the rolled-up tip-vortex structure, roll-up calculations need to be performed for the wake from the tip edges. Although the procedure for this tip-wake roll up is essentially the same as that used in the trailing-vortex-wake roll up, daunting complications arise from the numerical difficulties because the roll up of the tip-vortex wake occurs over the surface of the wing. As the tip-vortex wake rolls up in this model, it inevitably intersects with the wing surface, causing numerical problems. To bypass this difficulty, the separated-tip-flow model was developed with rigid tip wakes. Although this is not a correct representation of reality, this option was used solely to assess the effect of attached vs. separated tip flows on the prediction of LEV formation on the very low-AR wing case ($AR = 2$). As shown later in § 4.5, for this low-AR wing ($AR = 2$), the comparison of standard UVLM prediction for

LEV initiation with that from CFD was seen to have a noticeable discrepancy in contrast to the excellent correlation for all the other wings. This lack of agreement was traced to the strong effect of the separated tip flow by showing that the comparison with CFD improves when using the UVLM with the separated-tip-flow model. For all the other wings, no difference in the prediction was seen between the attached-tip-flow and separated-tip-flow models. This result can be understood by recalling that, from Prandtl's lifting-line theory, the induced downwash angle, α_i, for an elliptically loaded wing operating at a given lift coefficient, C_L, is inversely proportional to the aspect ratio (AR) as: $\alpha_i = C_L/\pi AR$ (see Anderson 2017, p. 444). For lower-AR wings, the tip vortices become stronger for a given lift coefficient, and they have a larger influence on the downwash over the wing. For this reason, the details of the modelled tip-vortex structure in the ULVM become more important at very low ARs and less important for higher ARs. Thus, except for the one exploratory study with the $AR = 2$ wing, the standard UVLM (without the wake roll up or the separated-tip-flow model) was used in all the studies in this effort.

3.1.2. *Calculation of spanwise variation of LESP*

Because the current effort explores the use of LESP to determine the initiation of LEV formation on a finite wing, an approach is needed to determine the spanwise variation of LESP along the wing at every time step. In the earlier work on the use of the LESP concept for LEV shedding on an airfoil, the chordwise variation of airfoil bound vortex-sheet strength was expressed as a Fourier series (2.1). As described in § 2.1, the instantaneous value of LESP was taken to be equal to the instantaneous value of A_0, because the A_0 term is the only one in (2.1) that accounts for the leading-edge suction. When the bound vorticity is modelled using a chordwise distribution of discrete-vortex rings, there is no A_0 term, and an alternate approach is needed to determine the LESP. In a vortex-lattice model, it is clear that the strength of the forward-most bound vortex leg is connected to the leading-edge vorticity in thin-airfoil theory and hence to the A_0 parameter. Direct use of the strength of this forward-most vortex leg, labelled as Γ_1 in this discussion and in figure 1, to calculate the LESP value is undesirable because the LESP value would then be dependent on the number of chordwise lattices used in the VLM discretization.

An approach for determining the value of LESP in a vortex-lattice method was developed by Aggarwal (2013), which is used in this effort. In this approach, it is assumed that on a small chordwise region near the leading edge occupied by the forward-most vortex lattice, all the terms in the Fourier series representation (2.1), except for the A_0 term, would be negligibly small since these coefficients anyway go to zero at the leading edge in thin-airfoil theory. With this assumption, the value of Γ_1 in the vortex-lattice representation can be connected to the A_0 value in thin-airfoil theory by equating the Γ_1 value to the integrated bound circulation strength due to the A_0 term over the chordwise extent of the forward-most lattice (from $x = 0$ at the leading edge to the aft end of the forward-most lattice, denoted here by Δx_1, shown in figure 1). The resulting equation is

$$
\begin{aligned}
\Gamma_1(t) = \int_0^{\Delta x_1} \gamma(x, t)\,\mathrm{d}x &= \int_0^{\cos^{-1}(1 - (2\Delta x_1/c))} \gamma(\theta, t)\frac{c}{2}\sin\theta\,\mathrm{d}\theta \\
&= \int_0^{\cos^{-1}(1 - (2\Delta x_1/c))} \left\{ 2U_\infty A_0(t)\frac{1 + \cos\theta}{\sin\theta} \right\}\frac{c}{2}\sin\theta\,\mathrm{d}\theta \\
&= cU_\infty A_0(t)\left[\cos^{-1}\left(1 - \frac{2\Delta x_1}{c}\right) + \sin\left\{\cos^{-1}\left(1 - \frac{2\Delta x_1}{c}\right)\right\}\right].
\end{aligned}
\tag{3.1}
$$

The resulting expression allows us to connect the A_0 value in thin airfoil theory with the Γ_1 value in the VLM as follows:

$$A_0(t) = \frac{\Gamma_1(t)}{U_\infty c \left[\cos^{-1}\left(1 - \frac{2\Delta x_1}{c}\right) + \sin\left\{\cos^{-1}\left(1 - \frac{2\Delta x_1}{c}\right)\right\} \right]}. \tag{3.2}$$

With this equivalence, the expression on the right side of (3.2) can be used to calculate the value of LESP in a VLM. This approach resulted in an LESP that was almost independent of the number of lattices along the chord – for a change from 10 to 200 lattices, the change in $A_0(t)$ was less than 0.005. However, the value was found to be short of the A_0 calculation in Ramesh *et al.* (2014) by approximately 13 %. To account for the differences between the two methods, (3.2) was modified by using a scaling factor of 1.13 on the right side, resulting in (3.3). As shown by Aggarwal (2013), this expression for A_0, calculated from a discrete-vortex-lattice approach, resulted in A_0 values that were invariant with the number of vortex lattices, and that consistently matched up with the A_0 values predicted by the method of Ramesh *et al.* (2014) for a range of airfoil motions.

$$A_0(t) = \frac{1.13\Gamma_1(t)}{U_\infty c \left[\cos^{-1}\left(1 - \frac{2\Delta x_1}{c}\right) + \sin\left\{\cos^{-1}\left(1 - \frac{2\Delta x_1}{c}\right)\right\} \right]}. \tag{3.3}$$

In the current implementation of the UVLM, the LESP(y, t) for each strip on a wing, located at spanwise coordinate y, is calculated by equating it to the $A_0(t)$ from (3.3), calculated using the Γ_1 for that strip at that time step in the calculation.

Because the UVLM assumes attached flow over the entire airfoil chord, the results from these predictions are valid only so long as there is no significant trailing-edge reversed flow and only until the initiation of LEV formation. In the current work, the UVLM is used to determine the initiation of LEV formation with the expectation that the predictions are likely to be poor when there is significant trailing-edge reversed flow preceding the LEV formation. An approach to extend the UVLM to handle wings with LEV formation using a vortex-sheet representation of the LEV sheet is presented in Hirato *et al.* (2019).

3.2. *CFD*

NCSU's REACTMB-INS solver is used for the CFD calculations performed in this study. This finite-volume solver formulates the time-dependent incompressible Navier–Stokes equations in an arbitrary Lagrangian/Eulerian (ALE) fashion. The ALE form enables moving-mesh flow simulations on the three-dimensional (3-D) body-fitted computational mesh. An incompressible version of Edwards' low-diffusion flux splitting scheme (LDFSS) (Cassidy, Edwards & Tian 2009) is used for discretizing inviscid fluxes in space. Discretization of viscous terms is performed using a second-order central difference method. The LDFSS method is extended to higher order of accuracy in space using the piecewise-parabolic method (Colella & Woodward 1984). For time integration, second-order temporal accuracy is achieved by using an implicit artificial compressibility method (Cassidy *et al.* 2009) with subiterations at each physical time step for continuity-equation convergence. A version of the Spalart–Allmaras one-equation eddy-viscosity model, modified by Edwards & Chandra (1996), is used for turbulence closure.

Figure 3 shows the representative mesh distribution for a rectangular half-wing used for the finite-wing calculations in the current work. The O-type mesh has 164 cells chordwise,
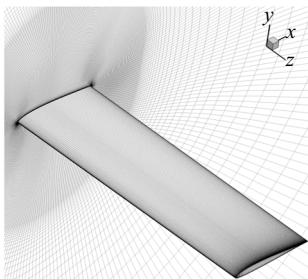
FIGURE 3. Representative mesh distribution for CFD analysis.

with finer resolution near the leading edge and trailing edge. The spanwise average spacing on the airfoil is chord/100, with finer resolution near the tip of the wing. The spanwise calculation domain extends two chord lengths beyond the tip of the wing, with an average spacing of chord/40 in this region. In the wall-normal direction, cell spacing starts 5×10^{-6} chords next to the wall, and has a growth factor of 1.15 moving away from the surface until the spacing reaches chord/100. From there, cell spacing is kept nearly uniform at chord/100 up to 1.3 chord from the surface. Then coarser meshes with a growth factor of 1.15 extend to 12 chord lengths away from the wing surface. Only the rectangular wing with an AR of 6 is shown here, but the general guidelines above are applied to meshes of all other wing geometries considered in this study.

The CFD model is validated by comparing the flow solution with the particle image velocimetry (PIV) results from the experimental study of Yilmaz & Rockwell (2012) for a rectangular flat plate with an AR of 2 undergoing a pitch-up motion, at a Reynolds number, *Re*, of 10 000, from $0°$ at $t^* = 0$ to $45°$ at $t^* = 4$, with the pitch angle being held at $45°$ thereafter until $t^* = 6$. Figure 4 compares predicted iso-surfaces of the second invariant of the velocity gradient tensor ($Q = 5$) with experimental images obtained from the PIV database. Side views of the 3-D streamline patterns at four instances in time are shown in figure 5. Compared with experimental data, the streamline patterns from CFD simulation show the same stage of development of the LEV at each time instant. Overall, the CFD results compare well with the PIV results, giving confidence in the utility of the CFD technique for the present work.

3.3. *Cases*

A total of 12 finite-wing geometries and two airfoil sections are considered in this effort. The two airfoil sections are the SD7003 (see Selig, Donovan & Fraser 1989) and a modified SD7003 with a sharpened leading edge having a 50 % reduction in the leading-edge radius compared to the original SD7003 airfoil. The two airfoil sections, referred to as the SD7003 and sharpened SD7003 in this article, are shown in figure 6.

The 12 finite-wing cases, labelled cases 1–12, have different taper ratios, tip-twist angles, sweep angles, ARs, non-dimensional pitch rates ($K \equiv \dot{\alpha} c / 2 U_\infty$, where $\dot{\alpha}$ is the pitch rate) and pivot locations (x_p), with sections formed using one or both the airfoils, SD7003 and sharpened SD7003. Table 1 lists the details of the two airfoil and the 12 finite-wing cases used in this paper. Figure 7 shows the nine wing geometries that are used in the 12 cases. The origin for the spanwise coordinate, *y*, is at the plane of symmetry of each wing, so that the left wing tip is at $2y/b = -1$, the root is at $2y/b = 0$ and the right wing tip is at $2y/b = 1$, where *b* is the wing span.
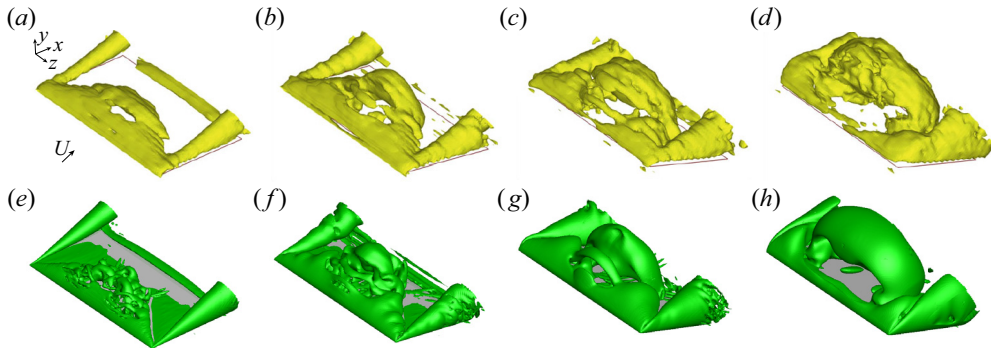
FIGURE 4. Volumes of iso-Q for four time instants during a pitch-up-and-hold motion. (*a–d*) PIV (experiment) (Yilmaz & Rockwell 2012), reproduced with permission. (*e–f*) CFD results. (*a,e*) $t^* = 2.4$, $\alpha = 27$ deg. (*b,f*) $t^* = 3.2$, $\alpha = 36$ deg. (*c,g*) $t^* = 4.0$, $\alpha = 45$ deg. (*d,h*) $t^* = 5.6$, $\alpha = 45$ deg.
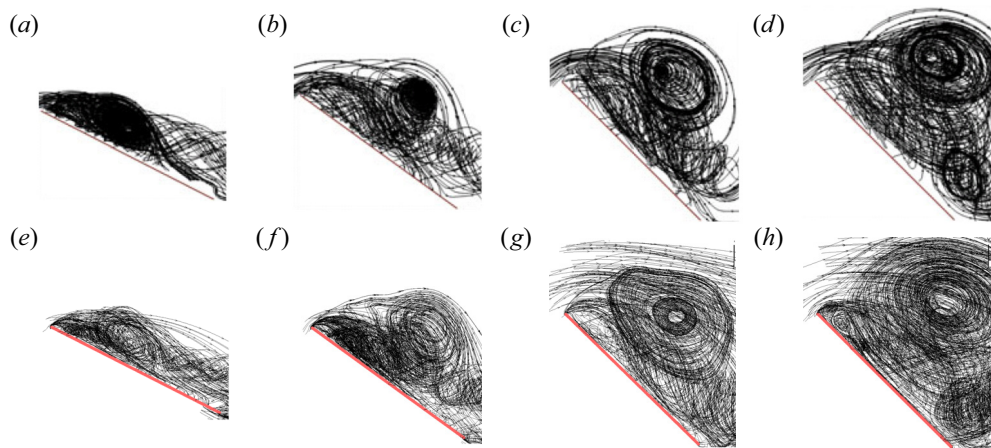

FIGURE 5. Side views of three-dimensional streamline patterns as a function of angle of attack. (*a–d*) PIV (experiment) images (Yilmaz & Rockwell 2012), reproduced with permission. (*e–h*) CFD results. (*a,e*) $t^* = 2.4$, $\alpha = 27$ deg. (*b,f*) $t^* = 3.2$, $\alpha = 36$ deg. (*c,g*) $t^* = 4.0$, $\alpha = 45$ deg. (*d,h*) $t^* = 5.6$, $\alpha = 45$ deg.

All the studies in this work have been performed for a chord Reynolds number of 20 000. This value was chosen because our previous studies have shown that the LESP criterion successfully predicts initiation of LEV formation on airfoils (in two-dimensional flow) at Reynolds numbers between 10 000 and 40 000. In this range of Reynolds numbers, the RANS CFD analysis using the Spalart–Allmaras turbulence model, as implemented in the REACTMB-INS flow solver, has also been shown to agree well with experimental results for LEV initiation and formation on airfoils (Ramesh *et al.* 2014). The only case with a non-constant chord is case 5; for this case, the leading edge has zero sweep, and the average chord (c_{ave}, at the $y = b/4$ location, where b is the wing span) has been used as the length scale to set the Reynolds number and the non-dimensional pitch rate, K. For the tapered wing (case 5), the pivot location for the pitching motion is at 25 % of the root chord at the $y = 0$ location, while for the swept wing (case 10), the pivot is at the quarter-chord location of the root section (at $y = 0$). The swept-wing geometry in case 10 has been defined using the airfoil section parallel to the plane of symmetry. Cases 11 and
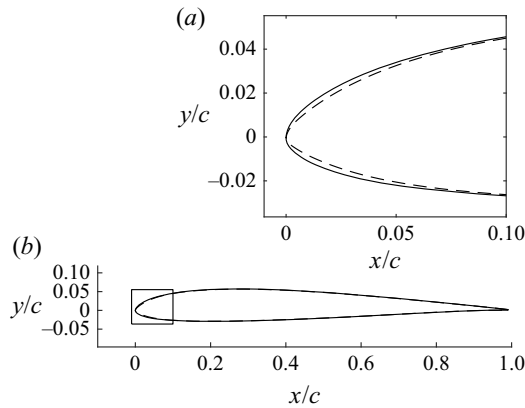
FIGURE 6. Comparison of the SD7003 (solid line) and the sharpened SD7003 (dashed line) geometries, with inset showing close-up view of the leading edge.

Case	Taper ratio	AR	Pitch rate K	Pivot point (x_p/c_{ave})	Tip twist (deg.)	Sweep angle (deg.)	Inboard incidence (deg.)	Airfoil
2D1	—	2D	0.3	0.25	—	—	0	SD7003
2D2	—	2D	0.3	0.25	—	—	0	Sharpened SD7003
1	1	6	0.3	0.25	0	0	0	SD7003
2	1	6	0.3	**0.75**	0	0	0	SD7003
3	1	6	**0.2**	0.25	0	0	0	SD7003
4	1	6	**0.4**	0.25	0	0	0	SD7003
5	**0.5**	6	0.3	0.25	0	0	0	SD7003
6	1	6	0.3	0.25	**10**	0	0	SD7003
7	1	**2**	0.3	0.25	0	0	0	SD7003
8	1	**4**	0.3	0.25	0	0	0	SD7003
9	1	**8**	0.3	0.25	0	0	0	SD7003
10	1	6	0.3	0.25	0	**30**	0	SD7003
11	1	6	0.3	0.25	0	0	**4**[a]	SD7003
12	1	6	0.3	0.25	0	0	0	**SD7003**[b]

TABLE 1. Test cases. Values in bold font indicate parameter changed from baseline case (case 1).
[a]Inboard third of wing has a 4° larger incidence compared to the rest of the wing.
[b]Inboard third of wing has the sharpened SD7003 airfoil, with the SD7003 used on the rest of the wing.

12 comprise wings that have abrupt changes in geometry demarcating the inboard third of the wing span from the outboard regions. Case 11 has a 4° higher incidence on the inboard third of the wing compared to the rest of the wing, and case 12 has the sharpened SD7003 airfoil over the inboard third of the wing and the original SD7003 section on the outboard portions.
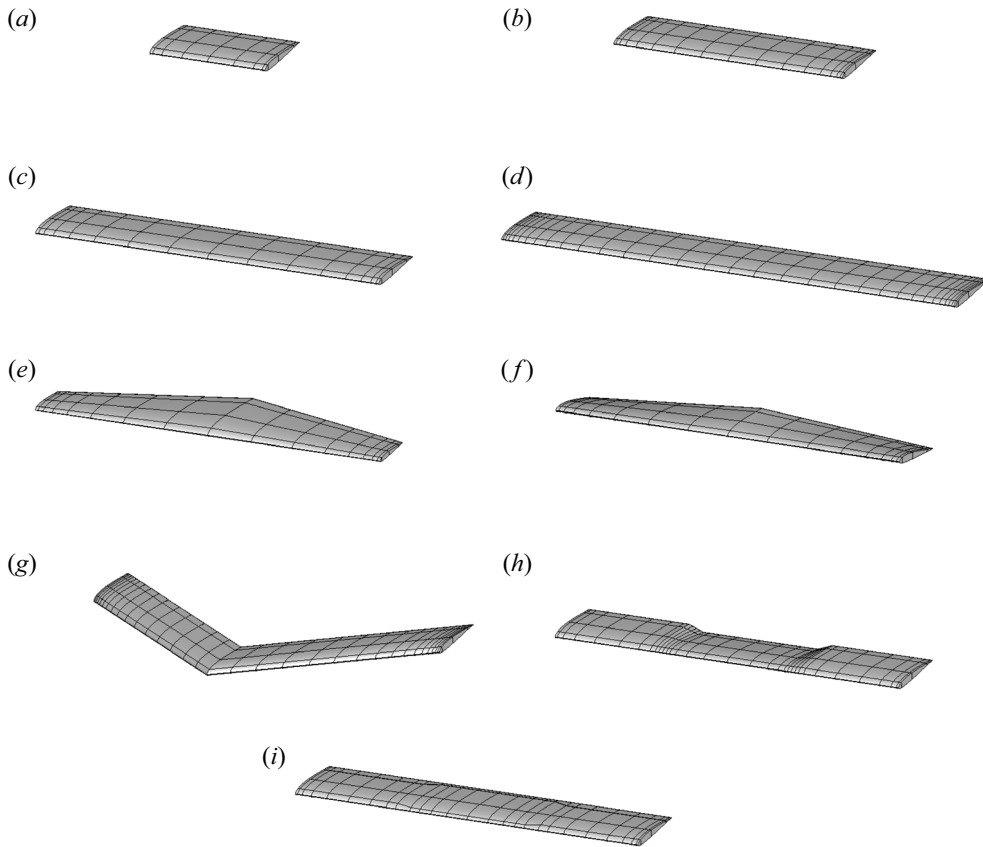
FIGURE 7. Geometries of the nine wings used in the 12 cases. (*a*) Rectangular wing ($AR = 2$) for case 7. (*b*) Rectangular wing ($AR = 4$) for case 8. (*c*) Rectangular wing ($AR = 6$) for cases 1, 2, 3, and 4. (*d*) Rectangular wing ($AR = 8$) for case 9. (*e*) Tapered wing for case 5. (*f*) Twisted wing for case 6. (*g*) Swept wing for case 10. (*h*) Rectangular wing with inboard third having larger incidence for case 11. (*i*) Rectangular wing with inboard third having sharpened leading edge for case 12.

3.4. *Motion parameters*

Although the LESP criterion has been verified for arbitrary pitching, plunging, surging and combination motions (Ramesh *et al.* 2013, 2014), the current work, owing to the large number of geometry cases, focuses on a pure pitching motion. Thus, for all wing geometries in this work, a 0–45° pitch-ramp motion is considered, with a non-dimensional pitch rate of $K = 0.3$ used in most cases, except for cases 3 and 4, which use $K = 0.2$ and 0.4, respectively. Figure 8 shows the time variations of the pitch angle, α (same as angle of attack in this work), for the three pitch rates. Non-dimensional time, t^*, is defined as $t^* \equiv U_\infty t / c_{ave}$. The equation for the pitch ramp motion is from Granlund *et al.* (2013).

3.5. *High-order prediction of LEV initiation from CFD*

An important element of the current work is the quantitative determination of the time instant of LEV initiation from our RANS CFD results. Although LEV initiation can be qualitatively inferred from CFD flow-field images by marking the time instant at which the first sign of an LEV structure appears during a motion, such a process is subjective
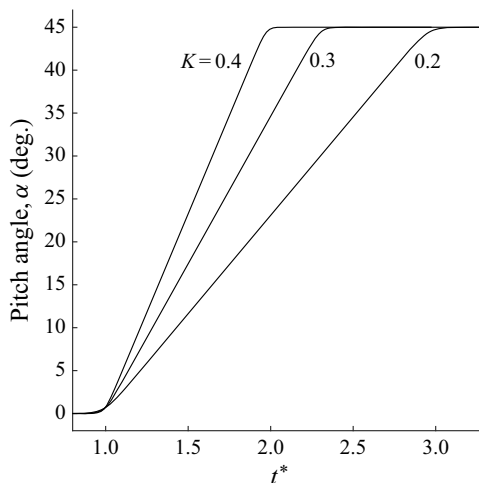
FIGURE 8. Pitch-angle time histories for $K = 0.2$, 0.3 and 0.4.

and results in noise when comparisons are made for a large number of cases. Further, it is desirable that the approach involve surface quantities and be straightforward to implement so that the data processing can be automated. In past research, experimental studies (Lorber, Carta & Covinno 1992; Schreck & Robinson 2005) have used the movement of the minimum-pressure location to track movement of the LEV, and the computational study of Ghosh Choudhuri *et al.* (1994) brought to light the behaviour of critical points in the velocity field near an LEV. Guided by these results in the literature, in our earlier work on LEV initiation on airfoils (Ramesh *et al.* 2014), we showed that a skin-friction signature near the leading edge from CFD results could be consistently used to identify LEV initiation. In the current work, we adapt this skin-friction signature to identify LEV initiation on finite-wing flows. In the remainder of this subsection, we discuss this skin-friction signature, first for airfoil flows and next for finite-wing flows.

3.5.1. *CFD prediction of LEV initiation on airfoils*

In order to provide an overview of the events leading up to LEV formation, as predicted by our RANS CFD method, figures 9(*a*)–9(*d*) show a series of representative CFD snapshots of streamlines and plots of the upper-surface skin-friction coefficient, C_f, for the SD7003 airfoil undergoing a pitch-up motion (case 2D1). The streamlines are drawn using flow velocity relative to the rotating frame of the body. As explained by Ghosh Choudhuri *et al.* (1994), the streamlines plotted using this reference frame have the intuitive advantage for physical interpretation of 'forward' and 'reverse' flow relative to the airfoil. In this frame of reference, the flow velocity is zero at the airfoil surface and the flow immediately adjacent to a point on the surface is either instantaneously moving forward (towards the trailing edge) or reverse (towards the leading edge). Skin-friction coefficient, C_f, calculated numerically in the CFD code, is defined as $C_f = \tau/[(1/2)\rho U_\infty^2]$, where τ is the surface shear stress. At the start of the pitching motion, the airfoil has attached flow over most of the upper surface, with the upper-surface C_f becoming negative past $x/c = 0.7$ indicating the presence of a small region of reversed flow over the aft 30 % of the chord in figure 9(*a*). At the higher pitch angle of 18.7°, as seen from figure 9(*b*), the trailing-edge reversed-flow region extends from $x/c = 0.5$. Of interest, however, is the tiny region near the leading edge over which C_f is negative, indicating the beginning of flow reversal at the
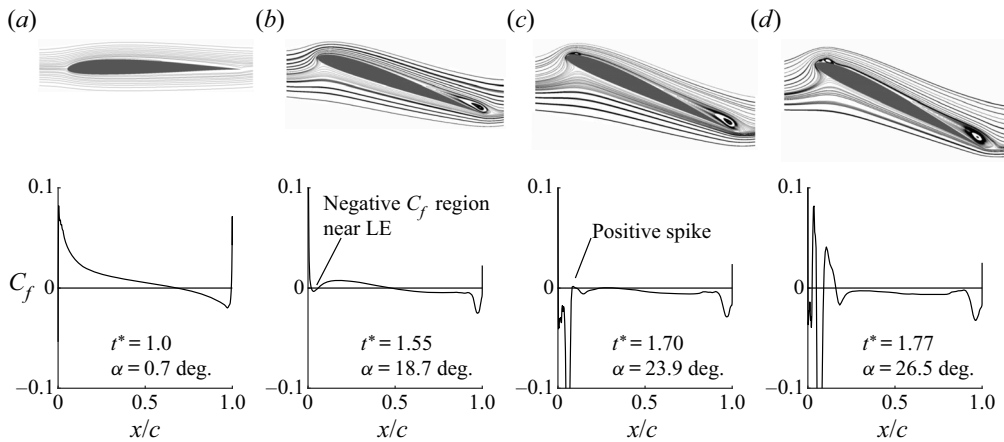
FIGURE 9. Sequence of events associated with LEV initiation on an airfoil: streamlines and C_f from CFD at different angles of attack. (*a*) Attached flow at the leading edge (LE). (*b*) Onset of reversed flow at LE. (*c*) Initiation of LEV. (*d*) Shortly after LEV initiation.

leading edge. At a higher pitch angle of 23.9°, the C_f distribution in figure 9(*c*) shows a positive spike reaching up to $C_f = 0$ within the negative-C_f region near the leading edge. In the approach developed in our earlier work (Ramesh *et al.* 2014), this first occurrence of positive C_f within the negative-C_f region near the leading edge is taken as the time instant corresponding to initiation of LEV formation. This C_f signature works consistently well for LEV identification from 2-D CFD solutions for the range of Reynolds numbers used in this and earlier work (Ramesh *et al.* 2014). Further, the CFD-predicted time instants for LEV initiation for a large set of unsteady airfoil motions were also shown in Ramesh *et al.* (2017) to qualitatively agree with experimental results from dye-flow visualization of the corresponding unsteady motions in water-tunnel experiments. This experimental confirmation was achieved by showing that, for each motion, there was a formation of a distinct LEV structure in the dye-flow visualization just after the time instant at which LEV initiation was observed from the surface-C_f signature in the RANS CFD result.

The LEV becomes discernible in the streamline plot at the higher pitch angle of 26.5° in figure 9(*d*), and clearly visible at even higher pitch angles (not shown). As the LEV grows, multiple vortices near the primary vortex are formed, resulting in the occurrence of several positive spikes within the negative-C_f region near the leading edge. In the current work, however, the focus is on the initiation of LEV formation rather than on the flow features that occur subsequent to LEV initiation. Although the overall observations presented here are somewhat specific to the RANS CFD method used in this work and earlier related efforts (Ramesh *et al.* 2013, 2014; Hirato *et al.* 2019), the structures observed in our CFD results are similar to those observed by Ghosh Choudhuri *et al.* (1994), and the overall observations are in general agreement with the LEV-formation flow physics discussed by other researchers (Visbal & Shang 1989; Ghosh Choudhuri *et al.* 1994; Mulleners & Raffel 2012; Gupta & Ansell 2019).

3.5.2. *Critical LESP for the two-dimensional cases 2D1 and 2D2*

The two airfoils used in the study, the original and the sharper leading-edge versions of the SD 7003, were studied for the pitching motions listed under cases 2D1 and 2D2 in table 1. For each case, results from two-dimensional CFD analysis were studied to determine the time instant and pitch angle for LEV initiation using the approach described
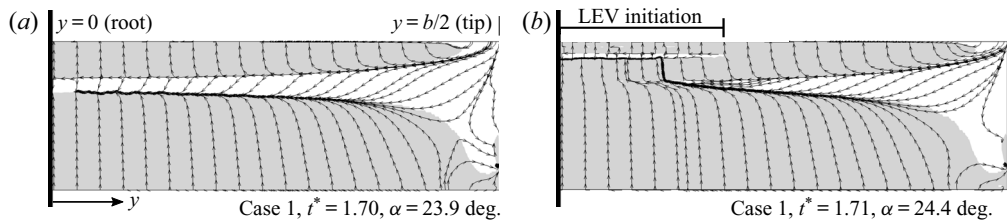
FIGURE 10. Upper-surface skin-friction lines from CFD for case 1. Right half of wing shown. In each snapshot, the leading edge is on the top and the trailing edge is on the bottom. Regions of the upper surface having negative chordwise component of skin friction are shaded in grey. (*a*) From CFD frame just prior to LEV initiation. (*b*) From CFD frame just after LEV initiation.

in § 3.5.1. The time variation of LESP for each case was determined using the unsteady thin-airfoil theory of Ramesh *et al.* (2014). From the results for case 2D1, the time instant, pitch angle and LESP at LEV initiation were found to be 1.70, 23.9° and 0.27, respectively. Similarly, the results for case 2D2 yield the time instant, pitch angle and LESP to be 1.61, 20.8°, and 0.24 at LEV initiation. Because case 2D2 uses the sharpened-leading-edge airfoil, the LEV initiation occurs at an earlier time in the motion. Thus, the LESP$_{crit}$ values for the SD7003 and the sharpened SD7003 airfoils, used in the remainder of this paper for low-order prediction of LEV initiation on finite wings, are 0.27 and 0.24.

3.5.3. *High-order prediction for wing illustrated using baseline wing (case 1)*

In extending the skin-friction signature for LEV initiation to finite-wing flows, we examine the CFD plots of the skin-friction lines on the upper surface at successive time instants. The objective is to find the time instant corresponding to the first occurrence of a region of positive skin friction within the negative skin-friction region near the leading edge. To illustrate the procedure, figures 10(*a*) and 10(*b*) show the upper-surface skin-friction lines on the baseline wing used in case 1 at two successive time instants from CFD output corresponding to just prior to LEV initiation and just after LEV initiation, respectively. These and all other skin-friction line plots are shown for the upper surface of the right side of the wing, i.e. for $0 \leqslant y \leqslant b/2$. The spanwise coordinate (y coordinate) and the root and tip locations, used in all the wings throughout the remainder of this article, are shown in figure 10(*a*). In these and subsequent upper-surface skin-friction plots, the regions of the upper surface having negative chordwise component of skin friction are shaded in grey. Figure 10(*a*) indicates that there are roughly four flow regions at $t^* = 1.70$: (i) a region of reversed flow, extending over approximately the first 15 % of the chord, with negative chordwise C_f, which is usually a precursor to LEV formation; (ii) a thin layer of reversed flow extending over the aft 60 % of the chord, indicating trailing-edge flow reversal; (iii) the triangle-shaped region at the right edge resulting from surface flow caused by the tip vortex; and (iv) the intermediate flow region with flow having a chordwise component that is from leading to trailing edge corresponding to positive chordwise C_f. It is noted that, for a section near the mid-span region (around $2y/b$ of 0), the chordwise C_f distribution on the upper surface resembles that seen for the 2-D case just prior to LEV formation in figure 9(*b*). In both these cases, there is a reversed-flow region over the aft portion of the airfoil (due to trailing-edge flow separation) and a reversed-flow region near the leading edge (which is the precursor to LEV initiation). In between these two reversed-flow regions is a region of forward flow.

Figure 10(b) shows the surface streamlines for the very next time instant ($t^* = 1.71$) from the CFD output for case 1. It is seen that there is a new region near the leading edge of the root area. This small region is the first occurrence of positive chordwise skin friction within the reversed-flow region near the leading edge. By analogy to the skin-friction signature in the airfoil case, it can be said that the t^* corresponding to LEV initiation for the finite-wing case 1 is between 1.70 and 1.71. It is also seen that the LEV initiation occurs at the wing root for this wing, i.e. at $2y/b = 0$, with the LEV starting to form over a spanwise region extending approximately from $2y/b = -0.35$ to 0.35. Thus in this work, we consider the time instant of LEV initiation for the baseline wing (case 1) as 1.71 with an error of 0.01, and the pitch angle for LEV initiation as 24.4° with an error of 0.5°.

3.6. *Low-order prediction of LEV initiation from UVLM*

The main hypothesis in the current research is that the same critical value of LESP that governs LEV initiation on a 2-D airfoil also determines the time instant and spanwise location of LEV initiation on a finite wing. This hypothesis forms the basis of the low-order prediction of LEV initiation on a finite wing using UVLM. In this methodology, the spanwise variation of LESP along the wing, determined using UVLM, is calculated at each time instant during an unsteady motion. At the first time instant when the LESP value at any location on the span equals the critical LESP for the 2-D airfoil section (determined *a priori* using 2-D CFD or experiment), LEV initiation is assumed to occur on the wing. Additionally, the spanwise location corresponding to where the local LESP just equals the 2-D critical LESP is taken as the spanwise location of LEV initiation on the wing. Note that, the low-order prediction uses input only from 2-D CFD (or experiment), and does not use any information from the finite-wing CFD predictions. If the hypothesis is correct, the time instant, pitch angle and spanwise location of LEV initiation as predicted by the low-order UVLM method will agree closely with those predicted independently for the same wing and motion by the high-order (CFD) approach. In this subsection, the low-order prediction approach is illustrated for the baseline-wing case 1. Further, the hypothesis is tested by comparing the results from the low-order prediction for this case with those from the high-order results from § 3.5.3.

3.6.1. *Low-order prediction illustrated using baseline-wing case 1*

Figure 11 shows the spanwise distributions of LESP for three values of t^* for case 1. The LESP distribution is seen to grow with increasing t^* because, for this range of t^* values, the wing is undergoing a pitch-up motion. Also plotted in the figure is a red horizontal line which corresponds to the LESP$_{crit}$ of 0.27 for the SD7003 airfoil. A red error bar is included to denote the error in the LESP$_{crit}$ of 0.03, determined for this airfoil in § 3.5.2. It is seen that, at t^* of 1.70, the maximum value of the UVLM-determined LESP distribution for the wing, which is at the wing root (at $y = 0$), just equals the 2-D LESP$_{crit}$ for the airfoil. Thus, using the hypothesis in § 3.6, the low-order prediction results in t^* of 1.70 and α of 24.2° for the LEV initiation for the baseline wing (case 1). These values compare excellently with the high-order predictions of t^* of 1.71 and α of 24.4° for this wing. Additionally, both methods predict that the spanwise location of LEV initiation corresponds to the wing root at $y = 0$. This excellent agreement shows that the low-order method is successful in predicting LEV initiation for the baseline-wing case 1, and verifies that the hypothesis of using 2-D LESP$_{crit}$ for low-order prediction of finite-wing LEV initiation has merit. In the following section, the hypothesis is further tested by comparing low-order and high-order predictions for all the remaining cases.
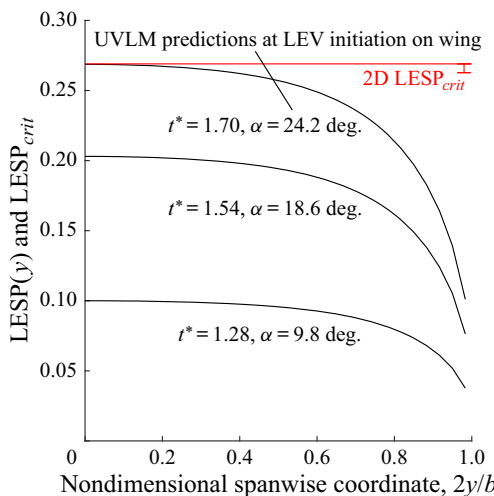
FIGURE 11. Spanwise variations of LESP from UVLM for three time instants for case 1, and LESP$_{crit}$ from 2-D CFD for the SD7003 airfoil.

4. Results

The initiation of LEV formation for all the cases listed in table 1 were calculated using both the low-order and high-order prediction approaches. The major advantage of the low-order prediction approach is that it uses a fast analysis method (the UVLM) and a single value of LESP$_{crit}$ obtained *a priori* from 2-D CFD or experiment (one for each airfoil used in the wing). Although we showed in § 3.6.1 that the low-order prediction of LEV initiation on the baseline wing (case 1) compared excellently with the high-order prediction, it is necessary to confirm if good agreement will also be seen for other wing geometries and motions.

The main objective of the study is to seek the answers to two key questions: (i) for each wing shape and motion, how well does the low-order prediction of time instant, pitch angle and spanwise location of LEV initiation agree with the high-order prediction? And (ii), how does LEV initiation vary with wing geometry and motion-kinematic parameters? With the aim of answering these questions, the results in this section are presented as eight case studies outlined in table 2. In each case study, case 1 is used as the baseline case for reference, and all the finite-wing results are compared with this case. For each case study, a single figure is used to compare the results from the high-order prediction with those from the low-order method. The high-order prediction for each wing will be presented as an upper-surface skin-friction plot at the instant of LEV initiation to show the t^*, α and spanwise location of LEV initiation. Comparison of this plot with that for the baseline wing in figure 10(*b*) will enable the determination of how the LEV initiation differs from that for the baseline case. These comparisons for all the case studies will be used to answer the second of the two key questions. The low-order prediction will be presented as the spanwise distribution of LESP for the wing at the t^* and α at which the LESP distribution first reaches the 2-D LESP$_{crit}$ value(s) for the airfoil(s) used in the wing. For comparison, this plot will also include the LESP distribution for the baseline case at LEV initiation, and horizontal lines to denote the 2-D LESP$_{crit}$ values for the airfoils. Comparison of the low-order predictions of t^*, α and spanwise location for LEV initiation with those predicted by the high-order method will enable assessment of the effectiveness of the low-order method, which will answer the first of the two key questions. Because the

Case study	Cases compared	Manipulated parameter
A	1, 2	Pivot location
B	1, 3, 4	Pitch rate
C	1, 5	Taper ratio
D	1, 6	Wing-tip-twist angle
E	1, 7, 8, 9	Aspect ratio
F	1, 10	Sweep angle
G	1, 11	Section incidence over inboard third of the wing
H	1, 12	Section leading-edge radius over inboard third of the wing

TABLE 2. Case studies.

low-order method uses only the 2-D LESP$_{crit}$ for predicting the LEV initiation on the finite wing, good comparison between the low-order and high-order results for all the case studies will demonstrate that the same LESP$_{crit}$ value that governs LEV initiation on a 2-D airfoil also determines the time instant and spanwise location of LEV initiation on a finite wing.

A summary of the results for all the cases is presented at the end of this section (in § 4.9) with two plots comparing low-order and high-order results for all the cases: the first plot comparing the pitch angle and the second plot comparing the spanwise location for LEV initiation. The discussion in § 4.9 also presents quantitative results to answer the two key questions posed earlier in this section. The numerical values for the t^*, α and spanwise location of LEV initiation from the low-order and high-order predictions for all the wings are tabulated in the Appendix.

4.1. *Case study A: effect of pivot location*

In case study A, the initiation of the LEV for case 2 (pivot at $x_p/c = 0.75$) is compared with the baseline case (case 1, pivot at $x_p/c = 0.25$) to study the effect of a change in pivot location. Figure 12 shows the comparison of results for the two pivot locations. The spanwise location for initiation of the LEV for case 2 (as deduced from the skin-friction plot in figure 12a) is similar to that for the baseline case 1 (figure 10b). The major difference from the baseline is that LEV initiation is delayed to a higher t^* and α due to motion-induced 'downwash' at the leading edge. This trend of delayed LEV formation with aft movement of the pivot point is not new. The trend and the reasoning have been reported by several researchers including Ham & Garelick (1968), Ericsson (1988), Visbal & Shang (1989), Visbal & Gordnier (1995), Ol (2009), Granlund, Ol & Bernal (2011) and Granlund *et al.* (2013).

In figure 12(b), the spanwise variation of LESP is shown to be nearly identical to that for the baseline. It is also seen that the low-order predictions for t^* and α for LEV initiation for case 2 agree well with the corresponding high-order predictions.

4.2. *Case study B: effect of pitch rate*

In case study B, the effect pitch rate on the initiation of the LEV is studied by comparing the results for cases 3 ($K = 0.2$) and 4 ($K = 0.4$) with those for the baseline case ($K = 0.3$). The results for this case study are shown in figure 13. The upper-surface skin-friction lines, plotted in figure 13(a), show that the LEV initiation for these two cases starts at the
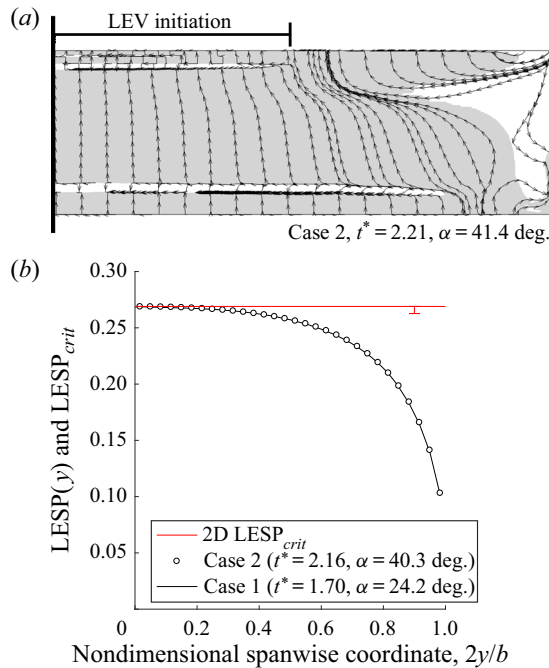
FIGURE 12. Case study A: effect of pivot location. (*a*) CFD result for LEV initiation for case 2. (*b*) UVLM prediction for LEV initiation for case 2 compared with case 1.

wing root like for case 1. It is seen that, with increasing pitch rate, the chordwise extent of the trailing-edge reversed-flow region progressively reduces. There is a small increase in α for LEV initiation with increase in pitch rate. Increase in pitch rate increases the motion-induced downwash at the leading edge, causing the small delay in LEV initiation. This trend between the pitch rate and the time instant of LEV onset is consistent with the features and explanations in the literature: Ham & Garelick (1968), Johnson & Ham (1972), McCroskey, Carr & McAlister (1976); McCroskey *et al.* (1981), McCroskey & Pucci (1982), Walker, Helin & Strickland (1985), Carr (1988), Visbal & Shang (1989), Acharya & Metwally (1992), Schreck & Helin (1994), Ghosh Choudhuri & Knight (1996), Lian (2009) and Jantzen *et al.* (2014).

Figure 13(*b*) shows the low-order predictions for the spanwise LESP distributions at LEV initiation for cases 3 and 4, which reach the 2-D LESP$_{crit}$ value at the wing root, indicating that the LEV initiation starts at the wing root. The low-order predictions for the t^* and α for LEV initiation are in reasonable agreement (within $1.6°$ for α) with the corresponding high-order predictions.

4.3. *Case study C: effect of taper ratio*

In case study C, the initiation of the LEV for the tapered wing of case 5 (taper ratio of 0.5) is compared with that for the baseline case (taper ratio of 1). From figure 14(*a*), it is seen that the CFD-predicted LEV initiation for case 5 starts at approximately $2y/b = 0.34$, which is similar to the observation of Spentzos *et al.* (2007) that LEV initiation on a tapered wing occurs between the wing root and tip (i.e. in the region $0 < 2y/b < 1$). Figure 14(*b*) compares the spanwise LESP distribution for case 5 with that for case 1. In contrast to the results for case 1, the spanwise LESP distribution for the tapered wing has a
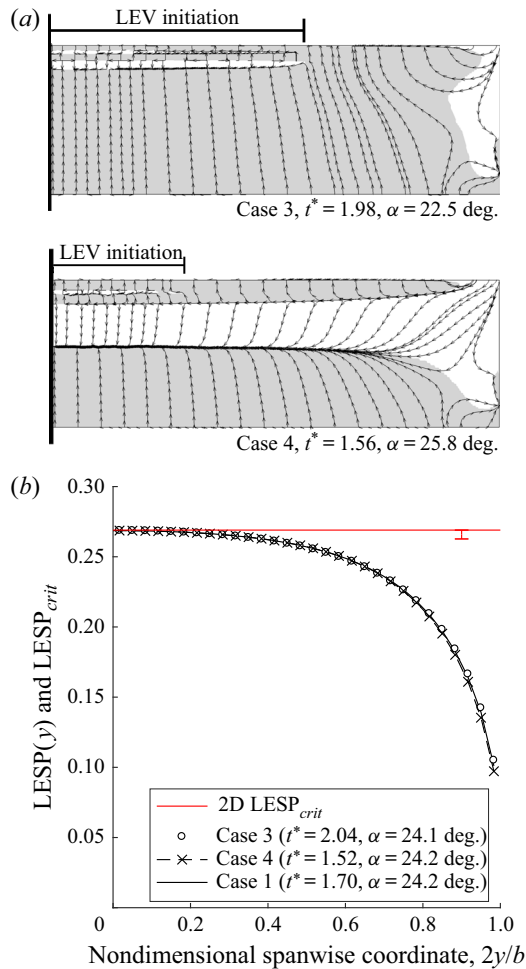
FIGURE 13. Case study B: effect of pitch rate. (*a*) CFD results for LEV initiation for cases 3 and 4. (*b*) UVLM predictions for LEV initiation for cases 3 and 4 compared with case 1.

maximum near $2y/b = 0.32$, which agrees well with the CFD-predicted spanwise location for LEV initiation. The t^* and α values for this low-order prediction also agree excellently with those from the high-order prediction.

4.4. *Case study D: effect of tip twist*

In case study D, the initiation of the LEV for the twisted wing with $10°$ tip twist (case 6) is compared with the results for case 1 (no tip twist). The twisted wing in case 6 has a linearly increasing section incidence angle from root to tip. The upper portion of figure 15 shows that the LEV starts forming for this wing from $2y/b$ of approximately 0.6. As seen from figure 15(*b*), the UVLM-predicted spanwise LESP distribution of case 6 has a clear maximum around the spanwise location of $2y/b$ of 0.6, which agrees excellently with the CFD prediction. The UVLM-predicted values for t^* and α for LEV initiation also agree excellently with the CFD prediction. It is also seen that the α for LEV initiation for case 6
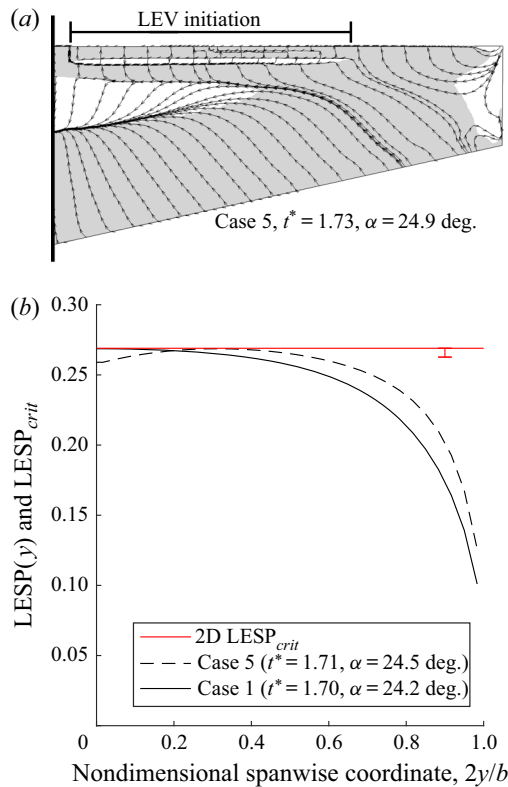
FIGURE 14. Case study C: effect of taper ratio. (*a*) CFD result for LEV initiation for case 5. (*b*) UVLM prediction for LEV initiation for case 5 compared with case 1.

is approximately $5°$ less than that for case 1. This early initiation of the LEV formation is the result of higher incidence of the outboard sections due to tip twist.

4.5. *Case study E: effect of AR*

In case study E, the initiation of the LEV for the rectangular wing cases 7, 8 and 9 ($AR = 2$, 4, 8, respectively) are compared with that for the baseline case (case 1, rectangular wing of $AR = 6$).

The AR effects on LEV initiation are presented in figure 16. Panel (*a*) shows the skin-friction plots for the rectangular wings with $AR = 2$, 4 and 8, respectively. These three plots indicate that the onset location of LEV initiation is at the wing root for all these wings. Also seen is that, although the region near the wing tip for each wing where the skin-friction lines are influenced by the tip vortex are roughly of the same size for these three wings, the fraction of the wing occupied by this region is clearly the largest for the $AR = 2$ wing. Thus it can be expected that the lower-AR wings will be more influenced by the tip-vortex effects. Figure 16(*b*) shows the spanwise distributions of LESP for the four cases: $AR = 2$, 4, 6 and 8. Each of the four cases has the maximum in LESP at the root, which agrees with the CFD-predicted root location for the onset of LEV formation for each wing. While the t^* and α values for LEV initiation for the $AR = 4$, 6 and 8 wings agree excellently with corresponding predictions from the high-order approach, the $AR = 2$ wing has CFD prediction for LEV initiation occurring at lower t^* and α
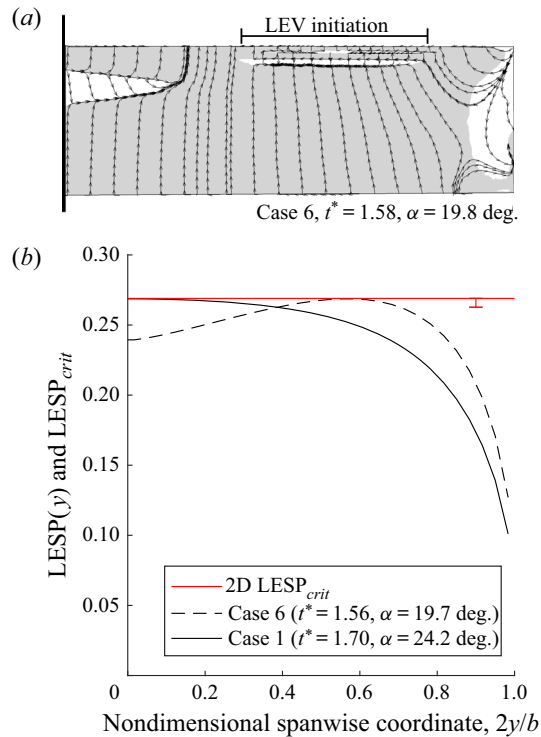
FIGURE 15. Case study D: effect of tip twist. (*a*) CFD result for LEV initiation for case 6. (*b*) UVLM prediction for LEV initiation for case 6 compared with case 1.

compared to the corresponding UVLM predictions. This discrepancy can be attributed to the increased effect of the 'lifted-up' tip-vortex structure on the downwash at the leading edge for the $AR = 2$ case due to the proximity of the tip vortex to the wing root. Because the UVLM does not take the lifting-up of the tip vortex into consideration, and instead assumes an attached tip vortex, the UVLM-predicted α for LEV initiation on the $AR = 2$ wing differs from the CFD prediction by almost $2.6°$.

To investigate the influence of the tip-vortex structure on the UVLM predictions, the UVLM code was used to study the $AR = 2$ (case 7) and $AR = 6$ (case 1) wings using the 'attached-tip-flow model, or ATFM' (figure 2*a*) and the 'separated-tip-flow model, or STFM' (figure 2*c*) options. Figure 17 presents the results from this study. It is seen that the t^* and α results for $AR = 6$ wing are mostly independent of the tip-flow model used. On the other hand, for the $AR = 2$ wing, the t^* and α predicted by the UVLM have better agreement with the CFD predictions when the separated-tip-flow model is used than when the attached-tip-flow model is used. This trend confirms the hypothesis that, for very low AR wings, it is important to capture the effects of the 'lifted-off' tip-vortex structure for improved predictions from the UVLM.

4.6. *Case study F: effect of sweep angle*

In case study F, the initiation of the LEV for the 30° swept-wing case 10 is compared with the baseline case (case 1, 0° sweep). It is to be noted that the pivot point for the swept wing is at the quarter-chord location of the root section. The top portion of figure 18 shows the
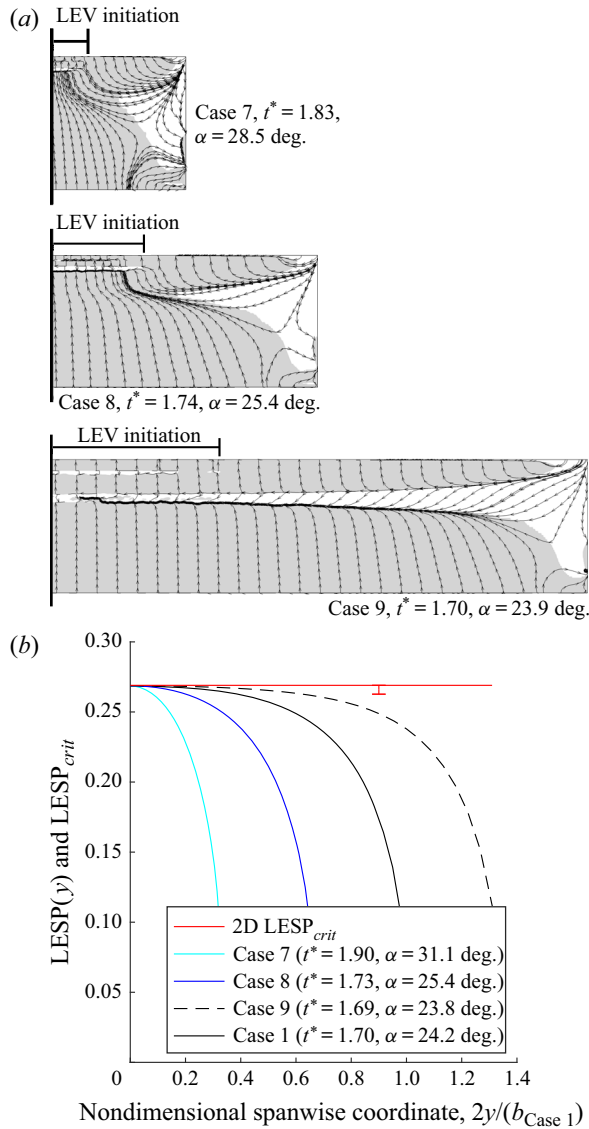
FIGURE 16. Case study E: effect of AR. (*a*) CFD results for LEV initiation for cases 7, 8 and 9. (*b*) UVLM prediction for LEV initiation for cases 7, 8 and 9 compared with case 1.

CFD-predicted skin-friction lines on the upper surface at LEV initiation. In contrast to the results for all the other wings, this swept-wing case exhibits LEV initiation that starts close to the wing tip, and at a very small α of 2.8°. The likely reason for this behaviour is that a pitch-up motion about the root quarter-chord location causes a significant motion-induced upwash towards the wing tips, causing the leading edge near the wing tip to become critical even at an early stage of the motion. The lower portion of figure 18 compares the spanwise distributions of LESP at LEV initiation for the swept wing and the unswept wing. It is seen that the LESP distribution for the swept wing is distinctly different from that for the unswept wing; it has a clear maximum near $2y/b = 0.9$, which shows that, like the high-order approach, the low-order approach also predicts LEV initiation very close to the
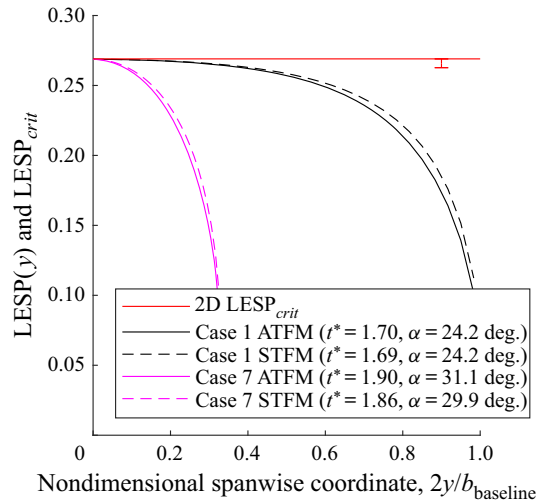
FIGURE 17. Comparison of UVLM predictions from attached-tip-flow model (ATFM) and separated-tip-flow model (STFM) for cases 1 and 7.

wing tip. It is seen that the low-order prediction for α is a small value of $1.5°$, which is within $1.3°$ of the CFD-predicted α. This discrepancy in the predicted α for LEV initiation between the two methods is higher than that for the other cases. One possible reason for this discrepancy is that, like with the $AR = 2$ wing, the LEV occurs very close to the tip vortex. Because the UVLM models the tip vortex using an 'attached-tip-flow' model (figure 2a), there is error in the predicted value of LESP near the wing tips. Another reason could be that spanwise pressure gradient or spanwise flow, which have both been discussed by other researchers in the context of LEV initiation (Lorber, Covino & Carta 1991; Ellington *et al.* 1996; Jones & Babinsky 2011), could be causing the discrepancy.

4.7. *Case study G: effect of abrupt change in incidence*

In case study G, the initiation of the LEV for case 11, for which the wing geometry has a $4°$ higher incidence over the inboard third of the span, is compared with that for case 1. The top portion of figure 19 shows the upper-surface skin-friction lines for case 11. This plot shows the abrupt change in sectional skin-friction lines at $2y/b = 0.33$, which is clearly related to the incidence change. It is seen that the LEV initiation for case 11 starts at the wing root, which is also to be expected owing to the increased incidence in that region. The lower portion of figure 19 shows the spanwise distributions of LESP for case 11 and the baseline case. It is seen that case 11 has a distinctly higher LESP over the inboard portion of the wing, resulting the low-order prediction for LEV initiation to occur at the wing root. It is also seen that the low-order and high-order predictions for α for LEV initiation on case 11 agree well with each other, and that case 11 has LEV initiation occurring approximately $4°$ earlier than case 1.

4.8. *Case study H: partially sharpened wing*

In case study H, the initiation of the LEV for case 12, in which the wing has a sharpened leading edge over the inboard third of the wing span, is compared with the baseline case 1.
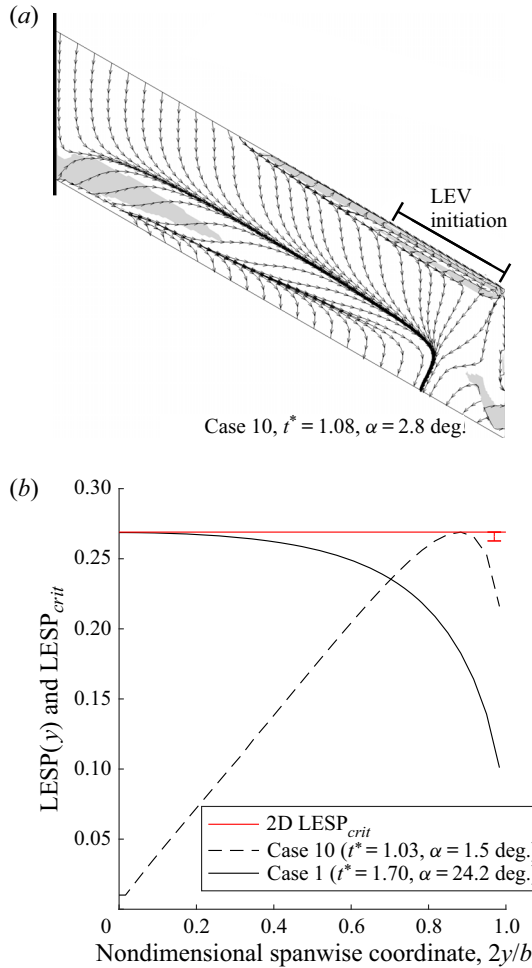
FIGURE 18. Case study F: effect of sweep angle. (*a*) CFD result for LEV initiation for case 10. (*b*) UVLM prediction for LEV initiation for case 10 compared with case 1.

The upper-surface skin-friction lines for case 12, in figure 20(*a*), shows that the LEV initiation starts at the wing root at α of 21.3°. Figure 20(*b*) compares the spanwise variation of LESP and LESP_{crit} for case 12 with the spanwise LESP for the baseline. Because of the abrupt change in airfoil between the inboard and the outboard portions of the wing, the 2-D LESP_{crit} value also changes from the value of $\text{LESP}_{crit} = 0.27$ for the SD7003 airfoil in the outboard portions to the value of $\text{LESP}_{crit} = 0.24$ for the sharpened SD7003 airfoil in the inboard portion. For case 12, an excellent agreement is seen between the low-order and high-order predictions for the t^* and α for LEV initiation. In contrast with case study G in which the abrupt change in section incidence caused a sudden change in the spanwise variation of LESP, the abrupt change in leading-edge radius in this case study causes an abrupt change in LESP_{crit}. Thus, while both cases 11 and 12 have a roughly 3–4° earlier LEV initiation compared to the baseline case, the earlier LEV initiation is achieved in different ways.
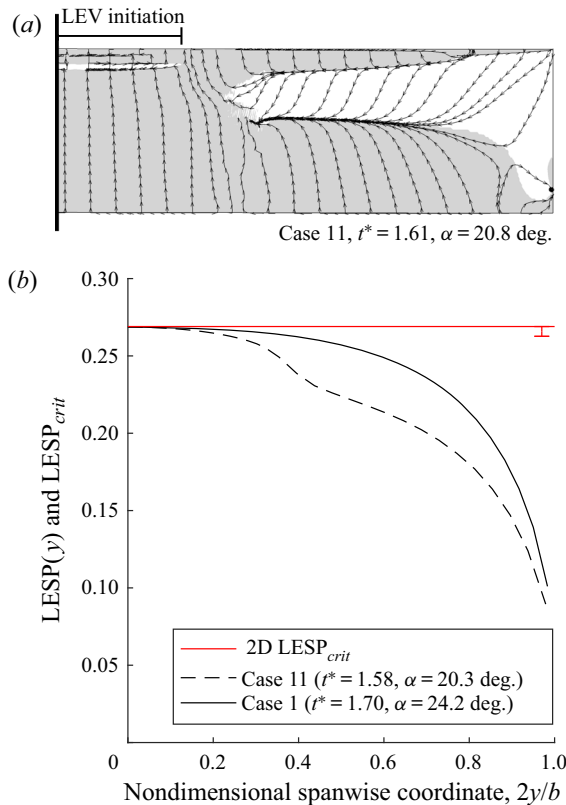
Case 11, $t^* = 1.61$, $\alpha = 20.8$ deg.

FIGURE 19. Case study G: partially deflected wing. (*a*) CFD result for LEV initiation for case 11. (*b*) UVLM prediction for LEV initiation for case 11 compared with case 1.

4.9. *Summary*

Figure 21 presents a comparison of low-order (UVLM) predictions for all the 12 finite-wing cases with the respective high-order (CFD) predictions. In figure 21(*a*), the α values for LEV initiation from UVLM are plotted against the CFD predictions as symbols for the 12 cases. The 45° line is co-plotted to denote perfect correlation, with the thickness of the line chosen to denote the CFD output resolution in α of $\Delta\alpha = 0.5°$, which is due to the difference in t^* of 0.01 between two successive time instants at which the skin-friction data are written out by the CFD code, an example of which is shown in figure 10. It is seen that the α for LEV initiation has a spread of almost 40° varying from 2.8° for case 10 to 41.4° for case 2. This large spread shows that criticality of α is not a good indicator for LEV initiation, as it varies significantly from case to case. In contrast, when the low-order prediction is made using the 2-D $LESP_{crit}$ value, the UVLM-to-CFD difference in α for LEV initiation is seen to be very good for all the cases as the symbols are all close to the 45° line. Among the cases considered, case 7 (the $AR = 2$ wing) has the maximum value of this UVLM-to-CFD difference in α of 2.6°, which is a result of the use of the attached-tip-flow model in the UVLM for a case in which tip-vortex effects are especially strong. Most of the other cases have much smaller UVLM-to-CFD differences; for all the other cases, the root-mean-square difference in α is 0.9° and the maximum difference is 1.6°. Figure 21(*b*) shows a plot of the low-order prediction of the spanwise location of LEV initiation against the corresponding high-order prediction, using symbols
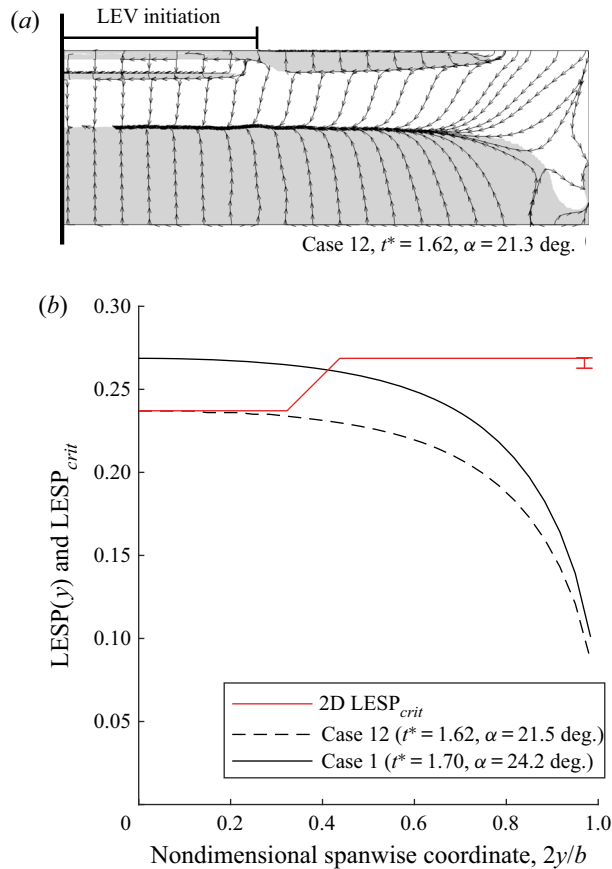
FIGURE 20. Case study H: partially sharpened wing. (*a*) CFD result for LEV initiation for case 12. (*b*) UVLM prediction for LEV initiation for case 12 compared with case 1.

to denote the 12 cases. In this figure too, the 45° line is plotted to show perfect correlation. The typical spanwise width over which LEV initiation was observed in the CFD for the 12 cases is shown as a horizontal error bar in the figure. It is seen that, although the spread for the spanwise locations ranges from the wing root ($2y/b = 0$) to almost the wing tip ($2y/b = 1$), the UVLM predictions for all cases agree remarkably well with the corresponding CFD observations. These excellent correlations in (i) α for LEV initiation, with a highest UVLM-to-CFD difference in α of 2.6° for cases that are spread over a range of 41.4°, and (ii) spanwise location with a highest UVLM-to-CFD difference in $2y/b$ of approximately 0.02 for cases that are spread over a range of $-0.87 < 2y/b < 0.87$ demonstrate the power of the LESP concept in predicting the LEV initiation on a range of finite-wing geometries using just the 2-D LESP$_{crit}$ values for the sections used in the wings along with a low-order method like the UVLM.

Although not presented here, the UVLM is capable of predicting forces and moments on the wing, which, as shown in Hirato (2016), agree well with CFD predictions in attached-flow conditions. Soon after the formation of an LEV or the occurrence of significant trailing-edge separation, the force predictions from the UVLM start to deviate from the CFD results.
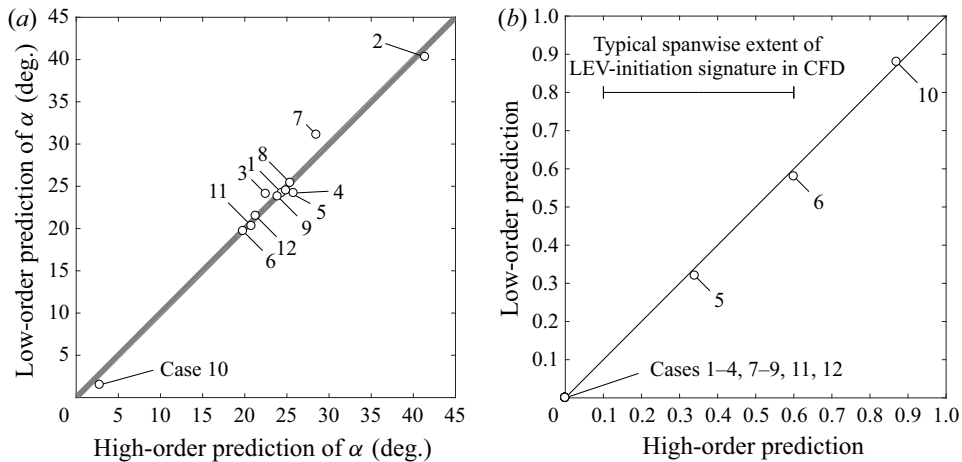
FIGURE 21. Comparison of low-order (UVLM) predictions with high-order (CFD) results for all the finite-wing cases. (*a*) Pitch angle at LEV initiation. (*b*) Spanwise location of LEV initiation.

5. Conclusions

This paper presents a study of the initiation of LEV formation on finite wings undergoing pitch-up motion. An important objective was to explore if criticality of leading-edge suction, which was shown in earlier work to be closely connected with LEV initiation on airfoils, would also determine LEV initiation on finite wings. A large set of wing cases undergoing pitching motion were studied using RANS CFD computations to determine the high-order predictions for pitch angle and spanwise location of LEV initiation. The same cases were also analysed using an unsteady vortex lattice method to determine the spanwise variation of the leading-edge suction parameter at every time step of the motion. The low-order prediction for LEV initiation is assumed to occur at the first time instant when the UVLM-predicted LESP value at any location on the span equals the critical LESP for the 2-D airfoil section (determined *a priori* using 2-D CFD or experiment). It was seen that the pitch angle and spanwise location for LEV initiation from the low-order prediction for all the finite-wing cases matched excellently with those obtained from the high-order predictions. For the 12 wing cases used in the paper, the maximum UVLM-to-CFD difference in pitch angle was $2.6°$ for cases having a spread of $41.4°$ in the pitch angle for LEV initiation. This result shows that it is possible to predict initiation of LEV formation on finite wings using a low-order method like a UVLM along with value(s) for the critical LESP for the airfoil(s) determined from two-dimensional CFD or experiments. Further, the low-order predictions for the spanwise locations for LEV initiation also agreed excellently with the CFD predictions in all cases.

While further refinement of the study is needed to better model the tip-vortex flow on low-AR wings in the UVLM formulation, the current results clearly show that the flow physics for initiation of LEV formation on finite wings is governed by a criticality of the LESP. During any motion, when the LESP on any spanwise portion of the wing reaches the critical value for that airfoil, LEV formation is initiated at that location. This criticality condition could be used to turn on and off LEV shedding in low-order prediction methods for finite wings with rounded leading edges. The insight from this research could also be used for LEV flow control to postpone or hasten LEV formation on various portions of a wing by controlling the LESP or critical LESP values.

Case	t^*		α (deg.)		$2y/b$	
	High-order	Low-order	High-order	Low-order	High-order	Low-order
1: Baseline	1.71	1.70	24.4	24.2	0.00	0.00
2: Aft pivot	2.21	2.16	41.4	40.3	0.00	0.00
3: $K = 0.2$	1.98	2.04	22.5	24.1	0.00	0.00
4: $K = 0.4$	1.56	1.52	25.8	24.2	0.00	0.00
5: Tapered	1.73	1.71	24.9	24.5	0.34	0.32
6: Twisted	1.58	1.56	19.8	19.7	0.60	0.58
7: $AR = 2$	1.83	1.90	28.5	31.1	0.00	0.00
8: $AR = 4$	1.74	1.73	25.4	25.4	0.00	0.00
9: $AR = 8$	1.70	1.69	23.9	23.8	0.00	0.00
10: Swept	1.08	1.03	2.8	1.5	0.87	0.88
11: Part twisted	1.61	1.58	20.8	20.3	0.00	0.00
12: Part sharpened	1.62	1.62	21.3	21.5	0.00	0.00

TABLE 3. Summary of LEV-initiation predictions for all the cases.

Acknowledgements

Declaration of interests

The authors report no conflict of interest.

Appendix. Summary of high-order and low-order predictions for all the cases

This appendix lists the numerical values for the t^*, α, and $2y/b$ predictions from the high-order and low-order methods for all the 12 finite-wing cases in table 3. These data were used in figures 21(*a*) and 21(*b*).

REFERENCES

ACHARYA, M. & METWALLY, M. H. 1992 Unsteady pressure field and vorticity production over a pitching airfoil. *AIAA J.* **30** (2), 403–411.

AGGARWAL, S. 2013 An inviscid numerical method for unsteady flows over airfoils and wings to predict the onset of leading edge vortex formation. Master's thesis, North Carolina State University.

ANDERSON, J. D. 2017 *Fundamentals of Aerodynamics*, 6th edn. McGraw-Hill Education.

ANSARI, S. A., ŻBIKOWSKI, R. & KNOWLES, K. 2006a A nonlinear unsteady aerodynamic model for insect-like flapping wings in the hover. Part 1. Methodology and analysis. *Proc. Inst. Mech. Engrs* **220** (2), 61–83.

ANSARI, S. A., ŻBIKOWSKI, R. & KNOWLES, K. 2006b A nonlinear unsteady aerodynamic model for insect-like flapping wings in the hover. Part 2. Implementation and validation. *Proc. Inst. Mech. Engrs* **220**, 169–186.

BEDDOES, T. S. 1978 Onset of leading-edge separation effects under dynamic conditions and low Mach number. In *34th Annual Forum of the American Helicopter Society*, vol. 17. American Helicopter Society.

BOTTOM, R. G. II, BORAZJANI, I., BLEVINS, E. L. & LAUDER, G. V. 2016 Hydrodynamics of swimming in stingrays: numerical simulations and the role of the leading-edge vortex. *J. Fluid Mech.* **788**, 407–443.

CARR, L. W. 1988 Progress in analysis and prediction of dynamic stall. *J. Aircraft* **25** (1), 6–17.

CASSIDY, D. A., EDWARDS, J. R. & TIAN, M. 2009 An investigation of interface-sharpening schemes for multiphase mixture flows. *J. Comput. Phys.* **228** (16), 5628–5649.

COLELLA, P. & WOODWARD, P. R. 1984 The piecewise parabolic method (ppm) for gas-dynamic simulations. *J. Comput. Phys.* **54**, 174–201.

CORKE, T. C. & THOMAS, F. O. 2015 Dynamic stall in pitching airfoils: aerodynamics damping and compressibility effects. *Annu. Rev. Fluid Mech.* **47**, 479–505.

DICKINSON, M. H. & GÖTZ, K. G. 1993 Unsteady aerodynamic performance of model wings at low Reynolds numbers. *J. Expl Biol.* **174**, 45–64.

EDWARDS, J. R. & CHANDRA, S. 1996 Comparison of eddy viscosity-transport turbulence models for three-dimensional, shock-separated flowfields. *AIAA J.* **34** (4), 756–763.

EKATERINARIS, J. A. & PLATZER, M. F. 1998 Computational prediction of airfoil dynamic stall. *Prog. Aerosp. Sci.* **33** (11–12), 759–846.

ELLINGTON, C. P. 1999 The novel aerodynamics of insect flight: applications to micro-air vehicles. *J. Expl Biol.* **202** (23), 3439–3448.

ELLINGTON, C. P., VAN DEN BERG, C., WILLMOTT, A. P. & THOMAS, A. L. R. 1996 Leading-edge vortices in insect flight. *Nature* **384**, 626–630.

ERICSSON, L. E. 1988 Moving wall effects in unsteady flow. *J. Aircraft* **25** (11), 977–990.

EVANS, W. T. & MORT, K. W. 1959 Analysis of computed flow parameters for a set of sudden stalls in low speed two-dimensional flow. *NACA Tech. Rep.* TN D-85. National Advisory Committee for Aeronautics.

FREYMUTH, P. 1988 Three-dimensional vortex systems of finite wings. *J. Aircraft* **25** (10), 971–972.

GAULT, D. E. 1957 A correlation of low-speed, airfoil-section stalling characteristics with Reynolds number and airfoil geometry. *NACA Tech. Rep.* TN 3963. National Advisory Committee for Aeronautics.

GHOSH CHOUDHURI, P. & KNIGHT, D. D. 1996 Effects of compressibility, pitch rate, and Reynolds number on unsteady incipient leading-edge boundary layer separation over a pitching airfoil. *J. Fluid Mech.* **308**, 195–217.

GHOSH CHOUDHURI, P., KNIGHT, D. D. & VISBAL, M. R. 1994 Two-dimensional unsteady leading-edge separation on a pitching airfoil. *AIAA J.* **32** (4), 673–681.

GORDNIER, R. E. & DEMASI, L. 2013 Implicit LES simulations of a flapping wing in forward flight. In *FEDSM 2013-16540. ASME 2013 Fluids Engineering Division Summer Meeting*. American Society of Mechanical Engineers.

GRANLUND, K., OL, M. & BERNAL, L. 2011 Experiment on pitching plates: force and flowfield measurements at low Reynolds numbers. *AIAA Paper* 2011-872.

GRANLUND, K. O., OL, M. V. & BERNAL, L. P. 2013 Unsteady pitching flat plates. *J. Fluid Mech.* **733**, R5.

GUPTA, R. & ANSELL, P. J. 2019 Unsteady flow physics of airfoil dynamic stall. *AIAA J.* **57** (1), 165–175.

GURSUL, I., GORDNIER, R. & VISBAL, M. 2005 Unsteady aerodynamics of nonslender delta wings. *Prog. Aerosp. Sci.* **41** (7), 515–557.

HAM, N. D. & GARELICK, M. S. 1968 Dynamic stall considerations in helicopter rotors. *J. Am. Helicopter Soc.* **13**, 49–55.

HARBIG, R. R., SHERIDAN, J. & THOMPSON, M. C. 2014 The role of advance ratio and aspect ratio in determining leading-edge vortex stability for flapping flight. *J. Fluid Mech.* **751**, 71–105.

HIRATO, Y. 2016 Leading-edge-vortex formation on finite wings in unsteady flow. PhD thesis, North Carolina State University.

HIRATO, Y., SHEN, M., GOPALARATHNAM, A. & EDWARDS, J. R. 2019 Vortex-sheet representation of leading-edge vortex shedding from finite wings. *J. Aircraft* **56** (4), 1626–1640.

HITZEL, S. M. & SCHMIDT, W. 1984 Slender wings with leading-edge vortex separation: a challenge for panel methods and euler solvers. *J. Aircraft* **21** (10), 751–759.

JANTZEN, R. T., TAIRA, K., GRANLUND, K. O. & OL, M. V. 2014 Vortex dynamics around pitching plates. *Phys. Fluids* **26** (5), 053606.

JOHNSON, W. & HAM, N. D. 1972 On the mechanism of dynamic stall. *J. Am. Helicopter Soc.* **17**, 36–45.

JONES, A. R. & BABINSKY, H. 2011 Reynolds number effects on leading edge vortex development. *Exp. Fluids* **51** (1), 197–210.

JONES, K. D. & PLATZER, M. F. 1998 On the prediction of dynamic stall onset on airfoils in low speed flow. In *Unsteady Aerodynamics and Aeroelasticity of Turbomachines* (ed. T. H. Fransson), pp. 797–812. Springer.

KATZ, J. 1981 A discrete vortex method for the non-steady separated flow over an airfoil. *J. Fluid Mech.* **102**, 315–328.

KATZ, J. & PLOTKIN, A. 2001 *Low-Speed Aerodynamics*, 2nd edn. Cambridge University Press.

LENTINK, D. & DICKINSON, M. H. 2009 Rotational accelerations stabilize leading edge vortices on revolving fly wings. *J. Expl Biol.* **212** (16), 2705–2719.

LENTINK, D., DICKSON, W. B., VAN LEEUWEN, J. L. & DICKINSON, M. H. 2009 Leading-edge vortices elevate lift of autorotating plant seeds. *Science* **324** (5933), 1438–1440.

LIAN, Y. 2009 Parametric study of a pitching flat plate at low Reynolds numbers. *AIAA Paper* 2009-3688.

LIMACHER, E., MORTON, C. & WOOD, D. 2016 On the trajectory of leading-edge vortices under the influence of coriolis acceleration. *J. Fluid Mech.* **800**, R1.

LIMACHER, E. & RIVAL, D. E. 2015 On the distribution of leading-edge vortex circulation in samara-like flight. *J. Fluid Mech.* **776**, 316–333.

LORBER, P. F., CARTA, F. O. & COVINNO, A. F. JR., 1992 An oscillating three-dimensional wing experiment: compressibility, sweep, rate, waveform, and geometry effects on unsteady separation and dynamic stall. *UTRC Tech. Rep.* R92-958325-6. UTRC.

LORBER, P. F., COVINO, A. F., JR. & Carta, F. O. 1991 Dynamic stall experiments on a swept three-dimensional wing in compressible flow. *AIAA Paper* 91-1795.

MALTBY, R. L. 1968 The development of the slender delta concept. *Aircraft Engng Aerosp. Technol.* **40** (3), 12–17.

MAXWORTHY, T. 1979 Experiments on the Weis-Fogh mechanism of lift generation by insects in hovering flight. Part 1. Dynamics of the 'fling'. *J. Fluid Mech.* **93**, 47–63.

MAXWORTHY, T. 2007 The formation and maintenance of a leading-edge vortex during the forward motion of an animal wing. *J. Fluid Mech.* **587**, 471–475.

MCCROSKEY, W. J., CARR, L. W. & MCALISTER, K. W. 1976 Dynamic stall experiments on oscillating airfoils. *AIAA J.* **14** (1), 57–63.

MCCROSKEY, W. J., MCALISTER, K., CARR, L. W., PUCCI, S. L., LAMBERT, O. & INDERGRAND, L. R. F. 1981 Dynamic stall on advanced airfoil sections. *J. Am. Helicopter Soc.* **26**, 40–50.

MCCROSKEY, W. J. & PUCCI, S. L. 1982 Viscous-inviscid interaction on oscillating airfoils in subsonic flow. *AIAA J.* **20** (2), 167–174.

MCCULLOUGH, G. B. & GAULT, D. E. 1951 Examples of three representative types of airfoil-section stall at low speed. *NACA Tech. Rep.* TN 2502. National Advisory Committee for Aeronautics.

MORRIS, W. J. & RUSAK, Z. 2013 Stall onset on aerofoils a low to moderately high Reynolds number flows. *J. Fluid Mech.* **733**, 439–472.

MUIJRES, F. T., JOHANSSON, L. C., BARFIELD, R., WOLF, M., SPEDDING, G. R. & HEDENSTRÖM, A. 2008 Leading-edge vortex improves lift in slow-flying bats. *Science* **319** (5867), 1250–1253.

MULLENERS, K. & RAFFEL, M. 2012 The onset of dynamic stall revisited. *Exp. Fluids* **52**, 779–793.

MURUA, J., PALACIOS, R. & GRAHAM, J. M. R. 2012 Applications of the unsteady vortex-lattice method in aircraft aeroelasticity and flight dynamics. *Prog. Aerosp. Sci.* **55**, 46–72.

OL, M. V. 2009 The high-frequency, high-amplitude pitch problem: airfoils, plates and wings. *AIAA Paper* 2009-3686.

POLHAMUS, E. C. 1966 A concept of the vortex lift of sharp-edge delta wings based on a leading-edge-suction analogy. *NASA Tech. Rep.* TN D-3767. National Aeronautics and Space Administration.

POLHAMUS, E. C. 1971 Prediction of vortex-lift characteristics by a leading-edge suction analogy. *J. Aircraft* **8** (4), 193–199.

RAMESH, K., GOPALARATHNAM, A., EDWARDS, J. R., OL, M. V. & GRANLUND, K. 2013 An unsteady airfoil theory applied to pitching motions validated against experiment and computation. *Theor. Comput. Fluid Dyn.* **27** (6), 843–864.

RAMESH, K., GOPALARATHNAM, A., GRANLUND, K., OL, M. V. & EDWARDS, J. R. 2014 Discrete-vortex method with novel shedding criterion for unsteady airfoil flows with intermittent leading-edge vortex shedding. *J. Fluid Mech.* **751**, 500–538.

RAMESH, K., GRANLUND, K., OL, M. V., GOPALARATHNAM, A. & EDWARDS, J. R. 2017 Leading-edge flow criticality as a governing factor in leading-edge vortex initiation in unsteady airfoil flows. *Theor. Comput. Fluid Dyn.* **32** (2), 109–136.

RAO, D. M. & CAMPBELL, J. F. 1987 Vortical flow management techniques. *Prog. Aerosp. Sci.* **24** (3), 173–224.

SCHRECK, S. & ROBINSON, M. 2005 Blade three-dimensional dynamic stall response to wind turbine operating condition. *J. Solar Energy Engng* **127** (4), 488–495.

SCHRECK, S. J. & HELIN, H. E. 1994 Unsteady vortex dynamics and surface pressure topologies on a finite pitching wing. *J. Aircraft* **31** (4), 899–907.

SELIG, M. S., DONOVAN, J. F. & FRASER, D. B. 1989 *Airfoils at Low Speeds. Soartech 8*. SoarTech Publications.

SPENTZOS, A., BARAKOS, G. N., BADCOCK, K. J., RICHARDS, B. E., COTON, F. N. & GALBRAITH, R. A. M. 2007 Computational fluid dynamics study of three-dimensional dynamic stall of various planform shapes. *J. Aircraft* **44** (4), 1118–1128.

TAYLOR, G. K., NUDDS, R. L. & THOMAS, A. L. 2003 Flying and swimming animals cruise at a Strouhal number tuned for high power efficiency. *Nature* **425** (6959), 707–711.

VENKATA, S. K. & JONES, A. R. 2013 Leading-edge vortex structure over multiple revolutions of a rotating wing. *J. Aircraft* **50** (4), 1312–1316.

VISBAL, M., YILMAZ, T. O. & ROCKWELL, D. 2013 Three-dimensional vortex formation on a heaving low-aspect-ratio wing: computations and experiments. *J. Fluids Struct.* **38**, 58–76.

VISBAL, M. R. & GORDNIER, R. E. 1995 Pitch rate and pitch-axis location effects on vortex breakdown onset. *J. Aircraft* **32** (5), 929–935.

VISBAL, M. R. & SHANG, J. S. 1989 Investigation of the flow structure around a rapidly pitching airfoil. *AIAA J.* **27** (8), 1044–1051.

WALKER, J. M., HELIN, H. E. & STRICKLAND, J. H. 1985 An experimental investigation of an airfoil undergoing large-amplitude pitching motions. *AIAA J.* **23** (8), 1141–1142.

WOJCIK, C. J. & BUCHHOLZ, J. H. J. 2014 Vorticity transport in the leading-edge vortex on a rotating blade. *J. Fluid Mech.* **743**, 249–261.

WONG, J. G. & RIVAL, D. E. 2015 Determining the relative stability of leading-edge vortices on nominally two-dimensional flapping profiles. *J. Fluid Mech.* **766**, 611–625.

YILMAZ, T. O. & ROCKWELL, D. 2012 Flow structure on finite-span wings due to pitch-up motion. *J. Fluid Mech.* **691**, 518–545.

YOUNG, J., LAI, J. C. & PLATZER, M. F. 2014 A review of progress and challenges in flapping foil power generation. *Prog. Aerosp. Sci.* **67**, 2–28.